J Mater Sci: Mater Med (2011) 22:237–245
DOI 10.1007/s10856-010-4206-2

Corrosion study of single crystal Ni–Mn–Ga alloy and $Tb_{0.27}Dy_{0.73}Fe_{1.95}$ alloy for the design of new medical microdevices

Pierre Pouponneau · Oumarou Savadogo · Teko Napporn · L'Hocine Yahia · Sylvain Martel

Received: 10 May 2010 / Accepted: 6 December 2010 / Published online: 11 January 2011

Abstract Once placed in a magnetic field, smart magnetic materials (SMM) change their shape, which could be use for the development of smaller minimally invasive surgery devices activated by magnetic field. However, the potential degradation and release of cytotoxic ions by SMM corrosion has to be determined. This paper evaluates the corrosion resistance of two SMM: a single crystal Ni–Mn–Ga alloy and $Tb_{0.27}Dy_{0.73}Fe_{1.95}$ alloy. Ni–Mn–Ga alloy displayed a corrosion potential (E_{corr}) of −0.58 V/SCE and a corrosion current density (i_{corr}) of 0.43 μA/cm^2. During the corrosion assay, Ni–Mn–Ga sample surface was partially protected; local pits were formed on 20% of the surface and nickel ions were mainly found in the electrolyte. $Tb_{0.27}Dy_{0.73}Fe_{1.95}$ alloy exhibited poor corrosion properties such as E_{corr} of −0.87 V/SCE and i_{corr} of 5.90 μA/cm^2. During the corrosion test, this alloy was continuously degraded, its surface was impaired by pits and cracks extensively and a high amount of iron ions was measured in the electrolyte. These alloys exhibited low corrosion parameters and a selective degradation in the electrolyte. They could only be used for medical applications if they are coated with high strain biocompatible materials or embedded in composites to prevent direct contact with physiological fluids.

P. Pouponneau · S. Martel (✉)
NanoRobotics Laboratory, Department of Computer and Software Engineering, Institute of Biomedical Engineering, École Polytechnique de Montréal (EPM), C.P. 6079, Succursale Centre-ville, Montréal, QC H3C 3A7, Canada
e-mail: sylvain.martel@polymtl.ca

O. Savadogo · T. Napporn
Laboratoire de Nouveaux Matériaux pour l'électrochimie et l'énergie, École Polytechnique de Montréal (EPM), C.P. 6079, Succursale Centre-ville, Montréal, QC H3C 3A7, Canada

P. Pouponneau · L'Hocine Yahia
Laboratory for the Innovation and Analysis of Bioperformance, Institute of Biomedical Engineering, École Polytechnique de Montréal (EPM), C.P. 6079, Succursale Centre-ville, Montréal, QC H3C 3A7, Canada

1 Introduction

Smart magnetic materials (SMM) by changing their shape in a magnetic field are very attractive materials for the development of smaller and more accurate minimally invasive surgery devices such as catheters, stents, and endoscopic robots [1]. In fact, a magnetic field can be used to activate parts of devices made of SMM such as tweezers, sensors, and release systems [2–4]. The magnetic activation avoids embedding batteries limiting the microdevices to several millimeters in size. In this context, medical microdevices propelled in the blood vessels by magnetic gradients generated by a clinical magnetic resonance imaging (MRI) system is currently in development by our team [5, 6]. The principle of magnetic propulsion has already been validated during in vivo assays [7]. This achievement reinforces our motivation to use SMM for the design of medical microdevices. However, the biocompatibility of SMM was not intensively investigated. The degradation of SMM by corrosion in physiological solution and the release of cytotoxic ions can limit their use for medical applications. In this paper, the corrosion resistance of two SMM, a single crystal Ni–Mn–Ga alloy, a magnetic shape memory alloy, and a giant magnetostrictive $Tb_{0.27}Dy_{0.73}Fe_{1.95}$ alloy is evaluated.

Ni–Mn–Ga alloys are thoroughly studied because of their magnetic shape memory properties [8, 9]. In a magnetic field, the strain can reach 6 to 10% depending of the

alloy structure [10, 11]. This property makes this alloy an ideal candidate for the realization of tweezers for autonomous medical microdevices. The corrosion behaviour of this alloy was previously investigated by three different teams [9, 12, 13]. Three main results were achieved: Ni–Mn–Ga alloys corrosion resistance depends on their structure [9]; the immersion of a single crystal Ni–Mn–Ga alloy in Hank's balanced salt solution for 12 h resulted in pits on the alloy surface [13]; the corrosion parameters of a polycrystal Ni–Mn–Ga alloy after a potentiodynamic corrosion assay in Hank's balanced salt solution were low and the sample surface was seriously impaired by cracks [12]. However, from our knowledge, no study has been done yet on the corrosion of the single crystal Ni–Mn–Ga alloys by potentiodynamic polarization assay and analysis of the corrosion electrolyte to identify the degradation products. Moreover, this work investigates the corrosion resistance of the single crystal Ni–Mn–Ga alloys because the single crystal structure could improve the corrosion properties in physiological solutions compared to those of polycrystal Ni–Mn–Ga [9]. $Tb_{0.27}Dy_{0.73}Fe_{1.95}$ alloy, known as Terfenold-D, is considered as the best giant magnetostrictive materials [14]. The magnestostriction, which is the natural strain of the alloy in a magnetic field can reach 2200 ppm [15]. For the medical applications, the magnetostrictive effect could be used for the development of sensors and drug release systems. From our knowledge, no study has been done yet on the corrosion behaviour of this alloy in physiological solutions.

In this paper, the corrosion resistance was studied by potentiodynamic polarization assay, surface analysis by atomic force microscopy (AFM), scanning electron microscopy (SEM) and corrosion electrolyte analysis by inductively coupled plasma time of flight mass spectrometry (ICP-TOF–MS). The results obtained in this preliminary study will be used to discuss the stability of these SMM in physiological solutions and their potential cytotoxic effects due to their degradation.

2 Materials and methods

2.1 Materials and sample preparation

The single crystal Ni–Mn–Ga samples with the following composition: 48.6 at% Ni, 31.5 at% Mn, 19.9 at% Ga, were provided by Dr Farrell (Defense Research Department and Development Canada) [16, 17]. The single crystal structure and the chemical composition were confirmed by X-ray diffraction (X'PERT, Philips) and energy dispersive spectrometry (EDS) (Inca, Oxford Instrument). The polycrystal giant magnetostrictive $Tb_{0.27}Dy_{0.73}Fe_{1.95}$ samples with the following composition: 67 at% Fe, 9 at% Tb, 24 at% Dy, were purchased from Gansu Tianxing Rare Earth Functional Material (China). All samples were mechanically polished with SiC wet paper (240 and 400 grits). Mirror finishing was obtained with alumina paste (15, 1, and 0.5 μm). $Tb_{0.27}Dy_{0.73}Fe_{1.95}$ cylinder samples (diameter 5 mm, height 5 mm) were placed directly after polishing in the sample holder of the corrosion setup. The dimensions of Ni–Mn–Ga samples, 8.14 × 7.46 × 4.75 mm (height × width × thickness), did not allowed the use of the sample holder. One surface of the sample was connected to a copper wire by a conductive tape. The wire and the sample were embedded in epoxy resin. The exposed surface of the sample was polished. The sample was then connected by the copper wire to the corrosion setup. The electrical contact was checked throughout all the steps of the sample preparation and the corrosion setup. Before the corrosion assay, the sample surface was cleaned with acetone, then with methanol.

2.2 Potentiodynamic polarization assay

This assay was done according to G5-94 standard of the American Society for Testing and Materials (ASTM) [18]. Cyclic polarization measurements were done using a standard three-electrode cell, a platinum grid as counter-electrode, and a saturated calomel electrode (SCE) as reference, with a microprocessor-controlled electronic potentiostat (model EG&G, Princeton Applied Research, model 273). The electrolyte was 500 mL of Hank's physiological solution (Sigma–Aldrich) with the following composition: NaCl: 8 g/L, KCl: 0.4 g/L, $NaHCO_3$: 0.35 g/L, KH_2PO_4: 0.006 g/L, Na_2HPO_4: 0.0475 g/L, glucose: 1 g/L, HEPES: 3.75 g/L. For 60 min, the solution was de-aerated with a strong flow of nitrogen gas. During the potentiodynamic polarization assay, the solution was maintained at 37°C under slow agitation and de-aerated by nitrogen gas bubbling. The sample was immersed in the Hank's solution and for 60 min the open circuit potential (E_{ocp}) was monitored. The potential scan was started at −250 mV under E_{ocp} value. The anodic potential value was increased at a constant rate of 0.17 mV/s up to 0.8 V/SCE. Then, the anodic potential value was decreased to E_{ocp} value at the same rate. The corrosion current density (i_{corr}, A/cm^2) at the corrosion potential (E_{corr}, V/SCE) was determined by Tafel extrapolation (CorrWare Version 2.9, Solartron Analytical). All potentials were expressed with reference to SCE. All the values were the mean of three measurements.

2.3 Surface analysis

The sample surface was characterized before and after the potentiondynamic polarization assays by several systems. SEM images were done using a Hitashi S-3500 N SEM.

AFM scans were done with a PicoSPM (Molecular imaging) to determine the sample topography. The tips were made of standard silicone. The surface analysis area was 30 μm × 30 μm and the surface was analysed three times. The average roughness was determined using the software embedded within the AFM system.

2.4 Inductively coupled plasma time of flight mass spectrometry

The supernatant and the precipitates taken from the corrosion solution were used for these analyses. Environmental grade HNO_3 (metals ions less than 100 ppb) was provided by Anachemia and 5% HNO_3 matrix was prepared with deionised ultra pure water (18.2 MΩ.cm). To insure the dissolution of any solid particles, 1.0 mL of concentrated nitric acid was added to 0.5 mL of each supernatant. Also, 0.2108 g of Ni–Mn–Ga precipitate was dissolved in 1.75 mL of concentrated nitric acid and 0.1623 g of $Tb_{0.27}Dy_{0.73}Fe_{1.95}$ precipitate was dissolved in 1.0 mL of concentrated nitric acid. The resulting solutions were diluted with 5% HNO_3 for the analysis. Ni, Mn, Ga, Tb and Dy were analyzed under hot plasma while, for Fe, cool plasma was preferred to minimize the interference of the ArO^+ at *m/z* 56. The analysis was performed with an ICP-TOF–MS model Renaissance axial from LECO [19]. Table 1 summarizes the conditions of cool and hot plasma experiments. To avoid detector overload under hot plasma conditions, ion deflection for N^+, O^+, H_2O^+, H_3O^+, N_2^+, O_2^+, O_2H^+, Ar^+, ArO^+, and Ar_2^+ were made. The liquid standards of Ni, Mn, Ga, Tb, Dy, and Fe were provided by Inorganicventures© and were used for the calibration. Before the calibration and the analyses, indium ion (contained in a so-called MassCal 10 standards) at a signal equal to *m/z* 115 was used in both plasma conditions (hot and cool) to optimize the system. Each analysis was repeated four times in order to insure its reproducibility.

Table 1 ICP-TOF–MS parameters

ICP source	Hot plasma	Cool plasma
Forward Power (kW)	1.4	0.75
Plasma flow (L mn^{-1})	14.2	15.8
Auxiliary flow (L mn^{-1})	0.8	1.1
Nebulizer flow (L mn^{-1})	0.9	1.1
Detector (V)	−2300	−2200

3 Results

3.1 Potentiodynamic polarization assay

Figure 1 and the data extracted from it (Table 2) show that the single crystal Ni–Mn–Ga alloy exhibited a corrosion potential of −0.58 ± 0.04 V/SCE and a corrosion current density of 0.43 ± 0.16 μA/cm^2. On the forward scan, the alloy exhibited passivation behavior between −0.431 and −0.184 V/SCE (Fig. 1). The breakdown potential (E_b) was −0.2 V/SCE. On the reverse scan, the curve displayed a hysteresis indicating pit formation on the sample surface [20]. The protection potential (E_p) was −0.4 V/SCE. For $Tb_{0.27}Dy_{0.73}Fe_{1.95}$ samples, the polarization curve started at very low potential, e.g. around −1.2 V/SCE (Fig. 1). E_{corr} was −0.87 ± 0.05 V/SCE and i_{corr} was 5.90 ± 0.41−μA/cm^2 (Table 2). During the forward scan, the curve had no passivation interval (Fig. 1). As a result, the sample did not form a protective layer on its surface. Moreover, the curve had a hysteresis on its reverse scan. During the reverse scan, the oscillations on the curve were attributed to the instability of the surface (Fig. 1). After a short decrease during the first 500 s, Ni–Mn–Ga E_{ocp} stayed stable at −0.63 V/SCE (Fig. 2). However, this value remained low. For $Tb_{0.27}Dy_{0.73}Fe_{1.95}$ alloy, E_{ocp} continuously oscillated due to the instability of the surface (Fig. 2). E_{ocp}

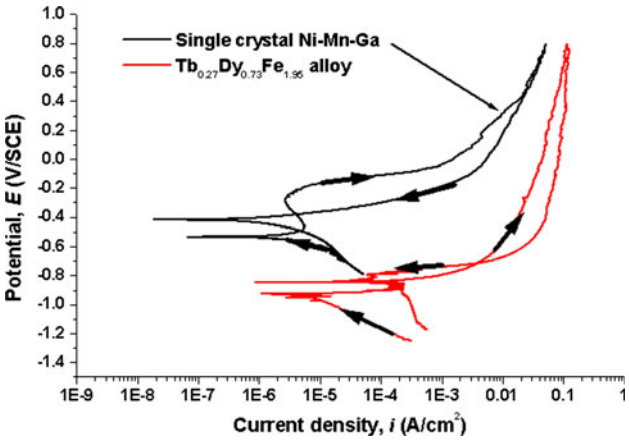

Fig. 1 Single crystal Ni–Mn–Ga alloy and $Tb_{0.27}Dy_{0.73}Fe_{1.95}$ alloy polarisation curves. *Arrows* indicate the increase and the decrease of the applied potential during the potentiodynamic polarization assay

Table 2 Corrosion parameters for the single crystal Ni–Mn–Ga alloy and $Tb_{0.27}Dy_{0.73}Fe_{1.95}$ alloy from the potentiodynamic polarization assay

Corrosion parameters	Single crystal Ni–Mn–Ga alloy	$Tb_{0.27}Dy_{0.73}Fe_{1.95}$ alloy
E_{corr} (V/SCE)	−0.58 ± 0.04	−0.87 ± 0.05
i_{corr} (μA/cm^2)	0.43 ± 0.16	5.90 ± 0.41

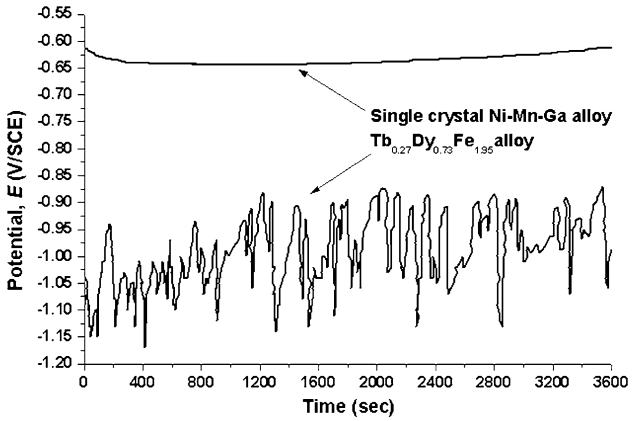

Fig. 2 E_{ocp} variation with time for single crystal Ni–Mn–Ga alloy and $Tb_{0.27}Dy_{0.73}Fe_{1.95}$ alloy

oscillations occurred on every assay and they cannot be attributed to problems related to the experimental corrosion setup. This E_{ocp} instability indicated that this alloy did not form a protective layer. Table 2 summarizes the corrosion parameters measured during the potentiodynamic polarization assay. The corrosion current density was much higher for $Tb_{0.27}Dy_{0.73}Fe_{1.95}$ alloy than the one for Ni–Mn–Ga alloy. Accordingly, $Tb_{0.27}Dy_{0.73}Fe_{1.95}$ alloy was very sensitive to the degradation. The corrosion rate was not determined for both alloys because these materials exhibited pitting corrosion behavior.

3.2 Surface analysis

After the corrosion assay, 80% of Ni–Mn–Ga alloy surface was not degraded and the surface has kept a mirror finishing as seen on SEM image (Fig. 3a). However, localised pits were formed and pits area represented approximately 20% of the sample surface. The width of the pits varied between 1.8 and 0.2 μm (Fig. 3b). The pits density in the attacked area reached 80 pits/μm^2. Before the corrosion assay, Ni–Mn–Ga sample surface was uniform without defects as confirmed by AFM image (Fig. 4a) and SEM images (images not shown). After the corrosion assay, the morphology of the sample surface has partially changed (Fig. 4b) and it was characterized by localised roughness. The localized roughness is attributed to the pits seen on SEM image (Fig. 3a). The AFM image (Fig. 4b) confirmed the distribution of localized pits. At the end of the corrosion assay, the sample roughness has increased to 168 nm (Table 3).

Before the corrosion assay, $Tb_{0.27}Dy_{0.73}Fe_{1.95}$ samples were polished several times to obtain an acceptable mirror finish surface. However, the morphology of the polished surface did not remain perfectly uniform as shown on AFM image (Fig. 6a). After the corrosion assay, the whole surface of $Tb_{0.27}Dy_{0.73}Fe_{1.95}$ alloy was seriously degraded and

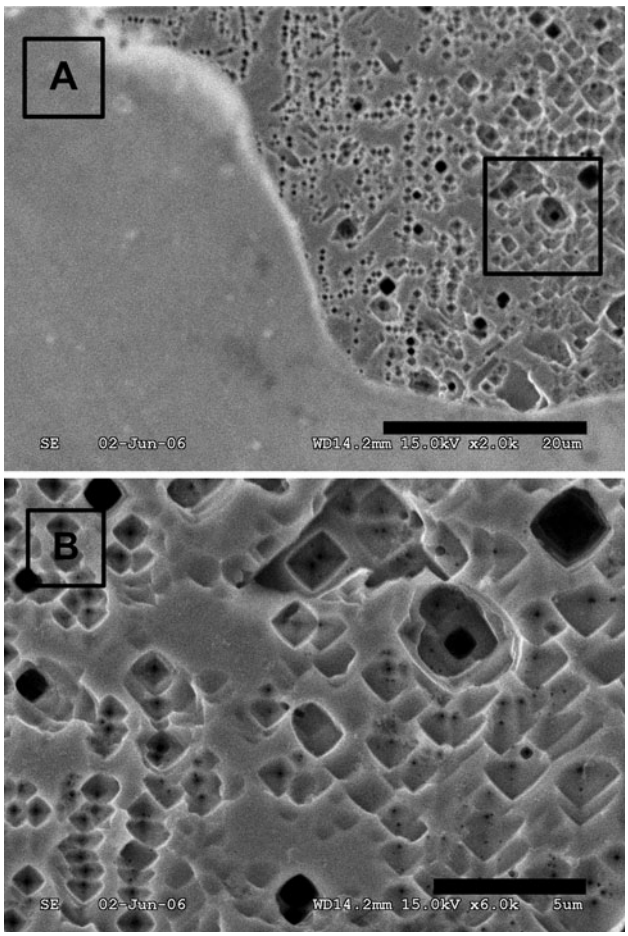

Fig. 3 Single crystal Ni–Mn–Ga SEM observations after the corrosion assay (**a** ×2000, *scale bar* 20 μm; **b** ×6000-Region of interest of image (**a**), *scale bar* 5 μm)

was characterized by the presence of pits and cracks (Fig. 5). The pits measured around 37 μm long and 18 μm deep (Fig. 5b). The length of the cracks varied from 500 to 100 μm and the width was between 71 and 30 μm (Fig. 5a). Moreover, the surface morphology has changed and exhibited various irregularities resulting from the degradation of the alloy (Fig. 6b). Accordingly, after the corrosion assay, the sample roughness of $Tb_{0.27}Dy_{0.73}Fe_{1.95}$ alloy has increased to 1410 nm (Table 3). This confirmed the high degradation of the surface.

3.3 ICP-TOF–MS analysis

Because of the sample fixture in the corrosion assay and the sample preparation, it was not possible to weight the sample at the end of the corrosion assay and then determine the sample weight loss. The chemical analysis of the electrolyte after the corrosion assay, using ICP-TOF–MS can be a good method to evaluate the degradation products of the two alloys. According to the ICP-TOF–MS analysis (Table 4), the single crystal Ni–Mn–Ga alloy dissolution

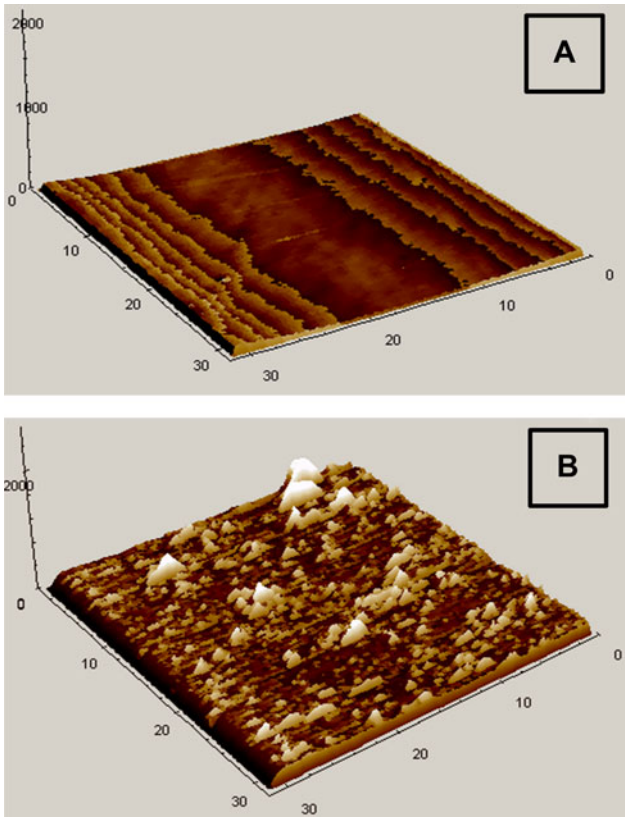

Fig. 4 Surface morphology obtained from AFM analysis of single crystal Ni–Mn–Ga sample **a** polished surface, **b** surface after the corrosion assay. The *scale* is in nm

Table 3 Surface average roughness increase of the single crystal Ni–Mn–Ga alloy and $Tb_{0.27}Dy_{0.73}Fe_{1.95}$ alloy after the potentiodynamic polarization assay

Sample	Roughness increase (nm)
Single crystal Ni–Mn–Ga alloy	168
$Tb_{0.27}Dy_{0.73}Fe_{1.95}$ alloy	1410

was not uniform. The manganese concentration in the supernatant was very high compared to that for Ni and Ga. Furthermore, the precipitates were mainly made of nickel (426 ppb) and gallium (293 ppb) and the manganese concentration remained very low (49 ppb). Accordingly, the single crystal Ni–Mn–Ga samples had released preferentially these two elements during the corrosion assay. As a consequence, the dissolution of the single crystal Ni–Mn–Ga did not occur according to the stochiometric proportions of the bulk alloy.

The concentration of iron found in $Tb_{0.27}Dy_{0.73}Fe_{1.95}$ alloy precipitates and the electrolyte supernatant remained much higher than the dysprosium and terbium concentrations (Table 5). Also, the dissolution of $Tb_{0.27}Dy_{0.73}Fe_{1.95}$ alloy did not occur according to the stochiometric

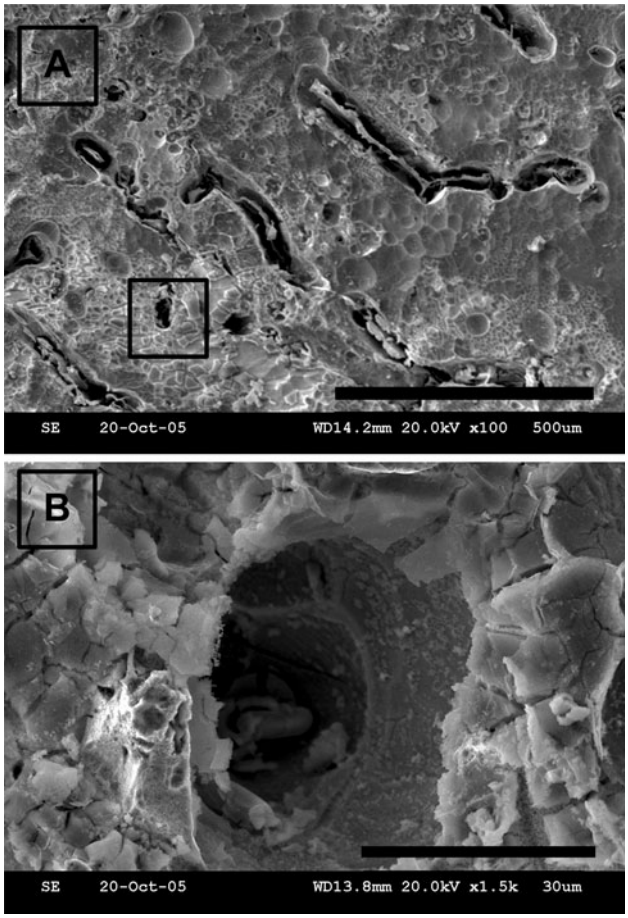

Fig. 5 $Tb_{0.27}Dy_{0.73}Fe_{1.95}$ SEM observations after the corrosion assay (**a** ×100, *scale bar* 500 μm; **b** ×1500-Region of interest of image (**a**), *scale bar* 30 μm)

proportions of the bulk alloy and iron was mainly released. The very low concentrations of iron, terbium and dysprosium measured in the electrolyte supernatant compared to those measured in the precipitates indicate that the $Tb_{0.27}Dy_{0.73}Fe_{1.95}$ degradation products remained principally as precipitates.

4 Discussion

Usually a metallic biomaterial exhibits the four following corrosion properties. A small passivation density current ensures the formation of an oxide layer on the surface. A low current density in the passive state induces a slow rate of metallic ion release. A high potential of pit formation indicates the resistance of the protective layer to the attacks from aggressive species. And finally, a large passivity interval indicates the stability of the protective layer on a large potential interval [21].

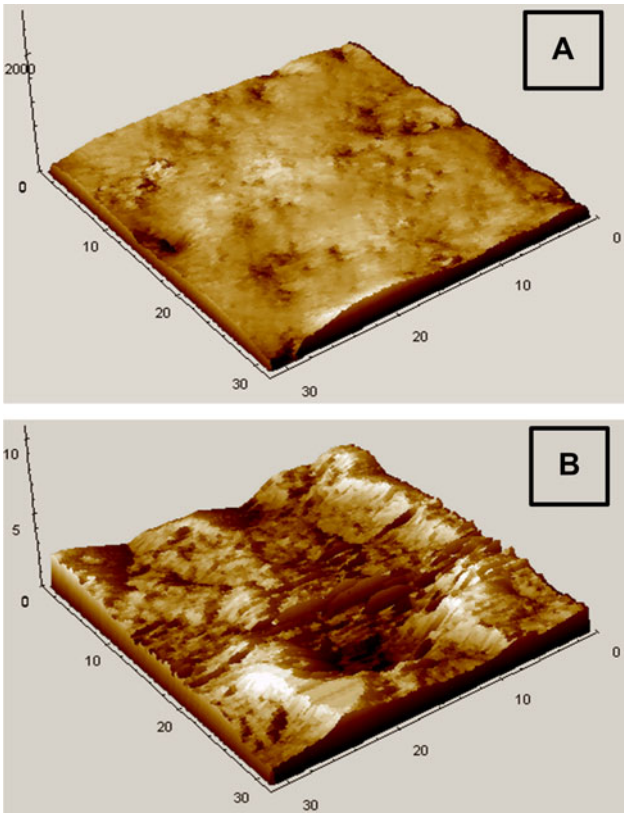

Fig. 6 Surface morphology obtained from AFM analysis of $Tb_{0.27}Dy_{0.73}Fe_{1.95}$ sample **a** polished surface, **b** surface after the corrosion assay. The *scale* is in nm

Table 4 ICP-TOF–MS analysis of corrosion electrolyte for the single crystal Ni–Mn–Ga alloy

Chemical element	Ni	Mn	Ga
Precipitates (ppb)	426	48	293
Corrosion electrolyte supernatant (ppb)	13	11	2

Table 5 ICP-TOF–MS analysis of corrosion electrolyte for $Tb_{0.27}Dy_{0.73}Fe_{1.95}$ alloy

Chemical element	Fe	Dy	Tb
Precipitates (ppb)	981	103	42
Corrosion electrolyte supernatant (ppb)	31	2	1

4.1 Ni–Mn–Ga alloy

Based on the above experimental results, single crystal Ni–Mn–Ga samples exhibited passivation behaviour on a short range of potential. Hence, this passivation was not enough to avoid surface degradation during the corrosion test, and localised pits were formed (Figs. 3, 4). The pit formation here may be attributed to the nickel which is known for its aptitude in creation of pits [22]. Furthermore the heterogeneous pitting behavior may be attributed to local martensite variants [16, 17] or to the presence of few twin boundaries [13] in the single crystal structure which exhibited poor corrosion resistance properties [9]. At the end of the corrosion assay, the small increase of the surface roughness confirmed the slight degradation of the surface. As a result, the main surface degradation mechanism for the single crystal Ni–Mn–Ga alloys is related to pit formation.

Corrosion assays were carried out on the single crystal alloy to evaluate the effect of the crystallography on the corrosion properties of Ni–Mn–Ga alloys in physiological solutions. In this work, three different results have confirmed that the single crystal Ni–Mn–Ga alloy exhibit better corrosion resistance than the polycrystal Ni–Mn–Ga alloy [12]. Firstly, the corrosion parameters determined on the single crystal Ni–Mn–Ga such as E_{corr} and i_{corr} were better than those obtained with the polycrystal Ni–Mn–Ga alloy (Table 6). Secondly, contrary to the single crystal Ni–Mn–Ga alloy, after the same corrosion assay, the entire surface of polycrystal Ni–Mn–Ga samples was seriously impaired by several cracks [12]. Thirdly, as shown in the results section, E_b and E_p for the single crystal Ni–Mn–Ga alloy were higher than those obtained with the polycrystal Ni–Mn–Ga alloy (E_b of -0.35 V/SCE and E_p of -0.7 V/SCE) [12]. The difference between E_b and E_p can be used to investigate the pitting corrosion resistance between two alloys [23]. In this case, the material exhibiting the smallest difference possesses the best pitting corrosion resistance. In our work, $E_b - E_p$ was smaller for the single crystal Ni–Mn–Ga alloy ($E_b - E_p = 0.2$ V/SCE) than for the polycrystal Ni–Mn–Ga alloy ($E_b - E_p = 0.35$ V/SCE). This result confirmed that the single crystal Ni–Mn–Ga exhibited better pitting corrosion resistance than the polycrystal Ni–Mn–Ga as found in [9]. Despite the partial protection of the single crystal Ni–Mn–Ga surface, its corrosion potential was lower than those of the current metallic alloys used in medical applications such as titanium or NiTi alloys (Table 6) [23]. Moreover, the susceptibility of the Ni–Mn–Ga alloy to form pits constitutes a

Table 6 Corrosion parameters of different materials tested in a Hank's solution

Materials	E_{corr} (V/SCE)	i_{corr} (μA/cm^2)	Reference
NiTi MP[a]	−0.19	0.07	[23]
Ti–13Nb–13Zr	−0.374	0.028	[20]
Ti–6Al-4 V	−0.407	0.019	[20]
$SmCo_5$	−0.650	246.3	[29]
Polycrystal Ni–Mn–Ga	−0.760	4	[12]
Nd–Fe-B	−0.822	5361	[29]

[a] *NiTi MP* NiTi mechanically polished

major limitation for biomedical applications because the pit formation is associated with a dissolution of the alloy in the body [12]. As a consequence, ICP-TOF–MS analysis was done to identify and quantify the ions released by the pit formation in the electrolyte. It was found that nickel ions were mainly released compared to gallium ions and manganese ions. For the duration of the reverse scan of the potentiodynamic polarization assay, pits were not passivated throughout a large potential range (Fig. 1) allowing a high rate of localized metal dissolution [24]. The high concentration of nickel ions measured in the electrolyte confirmed that this element might play a major role in the pit formation as it was also previously mentioned.

Before this corrosion study, a cell viability assay ((3-(4,5-dimethylthiazote-2yl)-2,5-diphenyl tetrazodium bromide) (MTT) assay) was done on the single crystal Ni–Mn–Ga alloy used in this work by indirect contact with mouse fibroblast cells L929 [25]. The cell viability, defined as the number of living cells in contact with the extracts of the single crystal Ni–Mn–Ga alloy divided by the number of living cells in their culture medium, decreased from 78 ± 3% at 24 h of incubation, to 18 ± 1% at 48 h and to 10 ± 1% at 72 h [25]. The decrease of the cell viability was attributed to the internalization of cytotoxic ions released by the material during the extraction. From the corrosion results, we could supposed that the high amount of nickel ions released due to the pitting corrosion was probably responsible for the decrease of the cell viability after 48 h because nickel ions can cross the cell membrane [26] after 24 h of incubation and then they can induce serious cytotoxic effects [27, 28]. Accordingly, we conclude that the single crystal Ni–Mn–Ga alloy can not be used for in vivo applications without surface treatment because of the pitting corrosion and the cytotoxic consequences on biological tissues.

4.2 $Tb_{0.27}Dy_{0.73}Fe_{1.95}$ alloy

$Tb_{0.27}Dy_{0.73}Fe_{1.95}$ alloy did not form a stable protective layer on its surface as confirmed by the potentiodynamic polarization assay (Fig. 1) and the E_{ocp} instability (Fig. 2) [29, 30]. Moreover, poor corrosion parameters were monitored (Table 2). As a consequence, $Tb_{0.27}Dy_{0.73}Fe_{1.95}$ alloy was corroded on its entire surface (Figs. 5, 6). Furthermore the degradation was not uniform and the corrosion products were mainly composed of iron (Table 6). Therefore, the corrosion behaviour of this alloy was attributed to the presence of a relatively high amount of iron (67%) which is known as an active metal. The presence of the hysteresis on the polarization curve (Fig. 1) was an indication of the pit formation. This is supported by some literature studies which have shown that Cl^- ions in the electrolyte attack the passive film and initiate the pit formation [31].

Compared to different metallic alloys (Table 6), $Tb_{0.27}Dy_{0.73}Fe_{1.95}$ alloy possesses the lowest corrosion parameters after the Nd–Fe–B alloy. The very low i_{corr} of Nd–Fe–B alloy ($i_{corr} = 5361\ \mu A/cm^2$) was attributed to the presence of the neodymium, a rare earth element [29]. From this observation, it can be concluded that the presence of rare earth elements in magnetic alloys limits the corrosion resistance for medical applications. Despite its low corrosion parameters, Nd–Fe–B alloys are used for dental prosthesis. In this case, the alloy is coated with parylene to avoid direct contact with the physiological solutions [32].

As for the single crystal Ni–Mn–Ga alloy, a MTT assay was performed on the same $Tb_{0.27}Dy_{0.73}Fe_{1.95}$ alloys used in this work by indirect contact [25]. After immersion in cell culture medium Dulbecco's Modified Eagle's Medium (DMEM) during 5 days for the preparation of the extracts, $Tb_{0.27}Dy_{0.73}Fe_{1.95}$ samples were slightly degraded and the surface was impaired [25]. However, the cell viability remained at 98 ± 1% at 24 h, 95 ± 6% at 48 h, and 92 ± 6% at 72 h. The corrosion study has shown that the degradation of $Tb_{0.27}Dy_{0.73}Fe_{1.95}$ alloy was characterized by a high amount of iron ions and in lesser proportion terbium and dysprosium ions in the electrolyte. Accordingly, the cell viability obtained with $Tb_{0.27}Dy_{0.73}Fe_{1.95}$ samples could be attributed to a less sensitivity of cells to terbium and dysprosium ions and the iron cytotoxic concentration was not reached. However, the cell viability assay and the corrosion assay have shown that $Tb_{0.27}Dy_{0.73}Fe_{1.95}$ alloy was seriously degraded in physiological solutions.

5 Conclusions

The corrosion resistance of the single crystal Ni–Mn–Ga alloy and the $Tb_{0.27}Dy_{0.73}Fe_{1.95}$ alloy was investigated to determine their stability in physiological solution and to evaluate their potential cytotoxicity. We found that despite a small passivation interval limiting the surface degradation of the single crystal Ni–Mn–Ga alloy, localised pits were formed during the corrosion assays and nickel ions with cytotoxic effects were mainly found in the electrolyte. Despite that the single crystal structure exhibited better corrosion resistance parameters compared to those obtained with the polycrystal structure, the corrosion parameters of the single crystal Ni–Mn–Ga alloy remained under those of metallic biomaterials. $Tb_{0.27}Dy_{0.73}Fe_{1.95}$ alloy exhibited lower corrosion parameters than those of the single crystal Ni–Mn–Ga alloy. This alloy was not able to form a protective layer. As a consequence, after the corrosion assay, the surface was seriously impaired by cracks and pits. The degradation of the $Tb_{0.27}Dy_{0.73}Fe_{1.95}$

alloy in the electrolyte was not uniform and a high amount of iron ions was measured. Both alloys cannot be considered as a biocompatible material because of their low corrosion parameters and their surface degradation. For medical applications, the single crystal Ni–Mn–Ga alloy and the $Tb_{0.27}Dy_{0.73}Fe_{1.95}$ alloy have to be coated to prevent direct contact with physiological fluids [32, 33]. In addition of its biocompatibility, the coating should have the appropriate strain to follow the magnetic strain. A good candidate will be elastomers [34]. An alternative solution will be the development of biocompatible smart magnetic composites based on these two alloys [35–37].

Acknowledgments This work was supported in part by the Canada Research Chair (CRC) in Micro/Nanosystem Development, Fabrication and Validation, the Canada Foundation for Innovation (CFI), the National Sciences and Engineering Research Council of Canada (NSERC), Fonds Québécois de la Recherche sur la Nature et les Technologies (FQRNT), Fonds de la Recherche en Santé du Québec (FRSQ) and the Government of Québec. The author acknowledges Stefania Polizu (EPM) for SEM images, Carole Massicotte and Josée Laviolette (EPM) for their help in the samples preparation, Edith Martin (EPM) for the training to the corrosion tests, Huimin Tian (EPM) for the AFM analysis, Shannon Farrell and Leon Cheng for Ni–Mn–Ga samples (Defense Research Department and Development Canada).

References

1. Lanfranco AR, Castellanos AE, Desai JP, Meyers WC. Robotic surgery: a current perspective. Ann Surg. 2004;239(1):14–21.
2. Abbott JJ, Nagy Z, Beyeler F, Nelson BJ. Robotics in the small. IEEE Robot & Automation Mag. 2007;14:92–103.
3. Li W, Guo W, Li M, Zhu Y, editors. A novel locomotion principle for endoscopic robot. 2006 IEEE International Conference on Mechatronics and Automation, ICMA 2006, Jun 25–28 2006. Luoyang, China.
4. Schurr MO. Robotics and telemanipulation technologies for endoscopic surgery. A review of the ARTEMIS project. Surg Endosc. 2000;14(4):375–81.
5. Pouponneau P, Leroux JC, Martel S. Magnetic nanoparticles encapsulated into biodegradable microparticles steered with an upgraded magnetic resonance imaging system for tumor chemoembolization. Biomaterials. 2009;30(31):6327–32.
6. Pouponneau P, Savadogo O, Napporn T, Yahia L, Martel S. Corrosion study of iron-cobalt alloys for MRI-based propulsion embedded in untethered microdevices operating in the vascular network. J Biomed Mater Res B Appl Biomater. 2010;93(1):203–11.
7. Martel S, Mathieu J-B, Felfoul O, Chanu A, Aboussouan E, Tamaz S, et al. Automatic navigation of an untethered device in the artery of a living animal using a conventional clinical magnetic resonance imaging system. Appl Phys Lett. 2007;90(11):114105.
8. Soderberg O, Ge Y, Sozinov A, Hannula S-P, Lindroos VK. Recent breakthrough development of the magnetic shape memory effect in Ni–Mn–Ga alloys. Smart Mater and Struct. 2005;14(5):223–35.
9. Liu XW, Soderberg O, Ge Y, Lanska N, Ullakko K, Lindroos VK, editors. On the corrosion of non-stoichiometric martensitic Ni–Mn–Ga alloys. J. Phys IV. 2003;112 (II):935–38.
10. Likhachev AA, Sozinov A, Ullakko K. Different modeling concepts of magnetic shape memory and their comparison with some experimental results obtained in Ni–Mn–Ga. Mater Sci Eng A. 2004;378(1–2 SPEC ISS):513–8.
11. Sozinov A, Likhachev AA, Lanska N, Ullakko K. Giant magnetic-field-induced strain in NiMnGa seven-layered martensitic phase. Appl Phys Lett. 2002;80(10):1746.
12. Martin E, Epure L, Manceur A, Savadogo O, Yahia LH, editors. Biocompatibility study of NI_2–MN–GA magnetic shape memory alloy for biomedical application. 7th Cansmart Workshop: Smart materials and structures; 21-22 October 2004; Montreal, Canada.
13. Stepan LL, Levi DS, Gans E, Mohanchandra KP, Ujihara M, Carman GP. Biocorrosion investigation of two shape memory nickel based alloys: Ni–Mn–Ga and thin film NiTi. J Biomed Mater Res A. 2007;82(3):768–76.
14. McMasters OD. Development, application, markets, and patent situation of magnetostrictive TERFENOL-D. J. Rare Earths. 1995;13:295–301.
15. Minagawa H, Kamada K, Nagai H, Nakata Y, Okutani T. Synthesis of $Tb_{0.3}Dy_{0.7}Fe_{1.9}$ magnetostrictive alloy by unidirectional solidification in magnetic field and microgravity. J Magn Magn Mater. 2002;248(2):230–5.
16. Cheng LM, Farrell SP, Ham-Su R, Hyatt CV. The influence of composition and thermomechanical treatments on the magnetic shape memory effect of Ni–Mn–Ga single crystals. Smart Structures and Materials 2004. Active Materials: Behavior and Mechanics, 15–18 March 2004; USA: SPIE-Int. Soc. Opt. Eng.
17. Farrell SP, Dunlap RA, Cheng LM, Ham-Su R, Gharghouri MA, Hyatt CV. Magnetic properties of single crystals of Ni–Mn–Ga magnetic shape memory alloys. Smart Structures and Materials 2004. Active Materials: Behavior and Mechanics, 15–18 March 2004; 2004; USA: SPIE-Int. Soc. Opt. Eng.
18. American Society For Testing and Materials. Annual Book of ASTM standard. Philadelphia, USA 2000.
19. Tian X, Emteborg H, Adams FC. Analytical performance of axial inductively coupled plasma time of flight mass spectrometry (ICP-TOFMS). J Ana At Spectrom. 1999;14(12):1807–14.
20. Starosvetsky D, Gotman I. Corrosion behavior of titanium nitride coated Ni–Ti shape memory surgical alloy. Biomaterials. 2001;22(13):1853–9.
21. De Assis SL, Wolynec S. Costa. Corrosion characterization of titanium alloys by electrochemical techniques. Electrochim Acta. 2006;51:1815–9.
22. Revie R. Uhlig's corrosion handbook. New York: John Wiley & Sons Inc; 2000.
23. Cisse O, Savadogo O, Wu M, Yahia LH. Effect of surface treatment of NiTi alloy on its corrosion behavior in Hanks' solution. J Biomed Mater Res. 2002;61(3):339–45.
24. Kaesche H. Corrosion of metals: physicochemical principles and current problems. Heidelberg, NY : Springer-Verlag; 2003.
25. Pouponneau P, Yahia LH, Merhi Y, Epure LM, Martel S. Biocompatibility of candidate materials for the realization of medical microdevices. 28th Annual International Conference of the IEEE Engineering in Medicine and Biology Society, EMBS'06, Aug 30-Sep 3 2006. NY, USA.
26. Barceloux DG. Nickel. J Toxicol Clin Toxicol. 1999;37(2):239–58.
27. Assis SL, Rogero SO, Antunes RA, Padilha AF, Costa I. A comparative study of the in vitro corrosion behavior and cytotoxicity of a superferritic stainless steel, a Ti-13Nb-13Zr alloy, and an austenitic stainless steel in Hank's solution. J Biomed Mater Res B Appl Biomater. 2005;73(1):109–16.
28. Chang LW (ed). Toxicology of metals: CRC Press, Inc.; 1996.
29. Gurrappa I. Corrosion studies related to suitability of permanent magnets for biomedical applications. Mater Charact. 2002;48(1):63–70.

30. Reclaru L, Luthy H, Eschler P-Y, Blatter A, Susz C. Corrosion behaviour of cobalt–chromium dental alloys doped with precious metals. Biomaterials. 2005;26(21):4358–65.
31. Sachdeva D, Balasubramaniam R. The effect of hydrogen on corrosion of $Tb_{0.3}Dy_{0.7}Fe_{1.92}$. J Electrochem Soc. 2008;155: C75–80.
32. Noar JH, Wahab A, Evans RD, Wojcik AG. The durability of parylene coatings on neodymium–iron–boron magnets. Eur J Orthod. 1999;21(6):685–93.
33. Yoshida M, Langer R, Lendlein A, Lahann J. From advanced biomedical coatings to multi-functionalized biomaterials. Polym Rev. 2006;46(4):347–75.
34. Strickler F, Richard R, McFadden S, Lindquist J, Schwarz MC, Faust R, et al. In vivo and in vitro characterization of poly(styrene-b-isobutylene-b-styrene) copolymer stent coatings for biostability, vascular compatibility and mechanical integrity. J Biomed Mater Res A. 2010;92:773–82.
35. Hosoda H, Takeuchi S, Inamura T, Wakashima K. Material design and shape memory properties of smart composites composed of polymer and ferromagnetic shape memory alloy particles. Sci Technol Adv Mater. 2004;5:503–9.
36. Min Z, Siu Wing O, Chan HLW. DC- and AC-magnetic field-induced strain effects in ferromagnetic shape memory composites of Ni–Mn–Ga single crystal and polyurethane polymer. J Appl Phys. 2010;107:09–942.
37. Kwon OY, Kim HY, Cha SI, Hong SH. Magnetostriction and magnetomechanical coupling of grain-aligned $Tb_{0.33}Dy_{0.67}Fe_y$/epoxy-filled composites. J Appl Phys. 2005;97(11):113905.